Reduction by Hydrogen of the Waste Rock Minerals Constituents of a Vanadium Ore

Túlio Simplício Ferreira[1], Isabel Cristina Braga Rodrigues[2], Adilson Lago Leite[3], Victor de Andrade Alvarenga Oliveira[*1]

[1]Thermal Analysis and Non-Ferrous Extractive Metallurgy Laboratory – Department of Metallurgical and Materials Engineering, Universidade Federal de Ouro Preto – Ouro Preto - Minas Gerais – Brazil – CEP 35400-000.

[2]Department of Chemistry, Biochemistry and Bioprocess Engineering - Universidade Federal de São João del-Rey, Ouro Branco, Minas Gerais, CEP 36497-899 – (ORCID 0000-0002-5474-6225).

[3]Geochemistry Laboratory – Department of Civil Engineering – Universidade Federal de Ouro Preto, Ouro Preto, Minas Gerais, CEP 35400-000, Brazil.

Abstract

A sample of vanadium ore has been characterized by X-ray diffractometry (XRD), scanning electron microscopy coupled with dispersive energy spectrometry (SEM-EDS) and thermogravimetric analysis (TG). The mineral composition was determined by the Rietveld method and the results showed that the major mineral constituents are maghemite (52.32%) and magnetite (15.73%). The SEM-EDS images showed that the vanadium is diffused over the crystal structure of almost all the minerals. Hydrogen reduction was assessed by thermogravimetry (TG), where three thermal events has been identified in the TG curves. The first event was probably related to two chemical reactions: (i) the oxidation of the mineral ulvospinel by different vanadium oxides, followed by the reduction of the products of this redox reaction by the hydrogen, and (ii) the reduction of the mineral magnesioferrite by the hydrogen. The other two events were attributed to the dehydroxylation of the phyllosilicates (greenalite, cronstedtite and sudoite) and the reduction of maghemite, magnetite, titanium oxides and vanadium oxides. Finally, the integration isoconversional method was used to determine the apparent activation energy (E_a), which ranged from 44.28kJ.mol^{-1} to 82.47 kJ.mol^{-1} for the Kissinger-Akahira-Sunose method (KAS), and from 33.44kJ.mol^{-1} to 65.54kJ.mol^{-1} for the Ozawa-Flynn-Wall method (OFW). These values imply that the reduction is controlled by mixed process for low conversion values (diffusion and chemical reaction are the controlling steps) and by chemical reaction for high conversion values.

Keyword: Isoconversional method; vanadium ore; reduction by hydrogen; kinetics

[*]Corresponding author: victor@ufop.edu.br

1. Introduction

The main application of vanadium is as an alloying additive to the steel-making process and the consumption of this element by this metallurgical sector corresponds to 85% of the worldwide production (Zhang et al., 2019; Gilligan and Nikoloski, 2020; Gasik, 2013; Moskalyk and Alfantazi, 2003). Minor amounts of vanadium (0.05-0.2%) reduces the particle grain size, increases hardenability, and improve the overall wear resistance. In addition, this element is also an important stabilizer for titanium and other special alloys (Zhang et al., 2019; Gilligan and Nikoloski, 2020; Gasik, 2013).

Vanadium is mostly commercially available as oxide (> 98% V_2O_5) (Zhang et a., 2019) or in ferrovanadium

alloys (40%, 60% or 80% of vanadium) (Moskalyk and Alfantazi, 2003). The primary sources of vanadium have a complex mineralogy (Liu et al., 2014; Sui et al., 2017) and substantial amounts of other metallic elements (e.g., Ti, Cr and Fe). It is worth to point out that a high chromium content in the ore leads to environmental and economical disadvantages, considering the fact that the presence of this element in the metallurgical waste increases the cost and restricts the possibilities of waste disposal (Peng, 2019; Wang et al., 2017). On the other hand, chromium and titanium can be recovered through the metallurgical process, to be sold as a by-product (Wang et al., 2017). Therefore, becomes imperative the development of alternatives for the vanadium extraction process aimed at the recovery of vanadium and other metallic elements.

Among many sources, it can be distinguished the vanadium titanomagnetite (VTM) as the primary source, metallurgical slags (containing 12-24 wt.% of V_2O_5) (Xiang et al, 2018; Wang et al., 2018; Zhang et al., 2019) and petroleum residues (Zhang et al., 2019; Xio et al., 2010). Most of the vanadium is now produced from the steel slag and many studies deals with the extraction of this element using direct leaching procedures, carbothermic reduction followed by magnetic separation and pyrometallurgical operations such as reduction, calcination and roasting followed by leaching with different chemical solutions (Wang et al., 2018).

Primary vanadium sources usually are submitted to a pyrometallurgical reduction step. The reduction of VTM concentrate is an essential step for the Blast Furnace (BF) process, reduction roasting magnetic separation and pre-reduction electric furnace melting process (Liu et al., 2014; Sui et al., 2017). Thus, the understanding of the reduction kinetics and reduction mechanisms of these ores is essential for developing new processes and techniques that promote a better use of these mineral resources.

In this research, the reduction of a vanadium ore sample was performed under low temperature (< 950 °C) in order to convert oxidized iron mineral phases into elemental iron (Fe^o), as a preparation for the subsequent hydrometallurgical acid leaching procedure. It is well known that the Fe^0 leaching is greatly faster and involves less aggressive conditions than those used for oxidized minerals iron phase.

2. Material And Methods

The vanadium ore sample has 100% particle size less than 75µm, and was oven dried for 24h at 105°C before being submitted to the experimental procedures. The sample was provided by the company Largo Resources and was obtained from a Brazilian mine located in the state of Bahia.

3. Chemical Composition

The major chemicals were determined on a solid blend composed of 0.2 g of ore and 4.0 g of a 1:1 mix of sodium carbonate (FMaia – 99.5%) and sodium tetraborate (Synth -99.5%). This mixture was then homogenized and melted in platinum crucible at 950°C for 30 minutes. After cooling in a desiccator, this mixture was completely dissolved using hydrochloric acid solution (≈16%). The major chemicals of the ore were then determined using inductively coupled plasma-optical emission spectrometry (ICP-OES – Varian 725-ES).

4. Mineral Composition

The mineral composition was determined using the x-ray diffraction (XRD) D2 Phaser (Bruker). The XRD patterns were compared with the ICSD standard incorporated into the Diffract. EVA software. The

Rietveld refinement method was carried out using the software TOPAS 5.0. The instrument settings, parameters, and references for the XRD analysis are shown in tables 1, 2 and 3, respectively.

Table 1. Instrument settings for XRD.

Diffractometer	Bruker D2 Phaser
Goniometer	Θ-2Θ, radius 141.1
Source	CuK_α (λ = 1.54184 Å)
Generator	30kV, 10mA
Sample	
Surface diameter (mm)	25
Spinning rate (rpm)	8
Preparation	Block loading
Incident optics	
Fixed divergence slit	0.6 mm
Receiving optics	
Soller slit	2.5
Detector	Lynxeye
Scan Info	
Angular range (2Θ)	15-70°
Step (2Θ)	0.18189
Length linear detector (2Θ)	5.002106
Time per step (s)	1.000
Measurement time (s)	3299

Table 2. Parameters used for quantitative analyses of XRD data.

Background	
Chebychev coefficients	6
1/x	Fitted for all
Profile function	Fundamental parameters
Cell parameters	Fitted for all phases
Crystallite size for each phase	Fitted the crystallite
Number of fitted parameters	~34

Table 3. References of the phase structures used for Rietveld analysis.

Phases	**COD – ID**	**Ref.**
Anatase	5000223	Horn et al., 1972
	7206075	Rezae et al., 2011
Clinopyroxene	9003349	Redhammer et al., 2004
Cronstedtite	9000019	Hendricks (1939)
Fayalite	9000559	Hazen (1977)
Greenalite	9000132	Shiruzu & Bailey, (1965)
Hematite	641734	TSV (1988)
Karelianite	9008083	Newnhen & Haan (1926)
Ilmenite	9008035	Barth (1934)
Indialite	9006271	Swartz (1994)
Iron	631734	Kim (1969)
Magnesioferrite	1011241 1011245	Barth (1932); Passereni, (1930)
Maghemite	9006317	Pecharromán (1995)
Magnetite	65339	Fleet (1986)
Melanovanadite	9010026	Konert & Evans (1987)
Pyrope	9001527	Ganguli & Cheng, (1994)
Rutile	9004144	Meager & Lager, (1979)
Spinel	9015716	Princivalle et al., (2012)
Sudoite	9000151	Eggleton & Bailey (1967)
Ti_7O_{13}	1008196	Page (1982)
Tistarite	9008082	Newnham, (19820
Tricalcium Silicate	9015421	GN (1975)
Ulvospinel	9013538 9013536	Bosi et al., (2009)

5. Thermogravimetric Analysis (Tg)

Approximately 75 mg of ore sample was submitted to thermogravimetric (TG) analyses using a Mettler Toledo apparatus (model Star System). High purity hydrogen (99.9990%) was applied as the reducing gas at a flow rate of 100 $mL.min^{-1}$. These quantities were chosen according to preliminary tests, which also demonstrated that under the experimental conditions, these variables have no influence on the TG curve pattern. The TG heating rates were 2.5°$C.min^{-1}$,

5°C.min^{-1}, 10°C.min^{-1}, 15°C.min^{-1} and 20°C.min^{-1} in the temperature range of 50°C to 950°C. All the gases used in the TG determinations were supplied by White Martins.

Scanning electron microscopy (sem) and energy dispersive spectroscopy (eds). Scanning Electron Microscopy (SEM) including Energy Dispersive Spectroscopy (EDS) were performed using a Tescan equipment, model VEGA 3 LMH, coupled to an EDS INCA x-act, model 51-ADD0007. All the ore samples were embossed using a commercial polyester resin, to be after polished using sandpaper of different grit sizes. The polishing finishing was done using 1.0 μm alumina paste. Subsequently the samples were covered with gold by sputtering techniques.

6. Reduction Tests

Reduction tests were performed on 5 g ore samples using a rotary kiln (20 rpm). Tests conditions were temperatures of 420°C, 520°C and 950°C; flow rate of 1 L.min^{-1} for 1h. Hydrogen (99.9990%) was used as the reducing gas where the flow rate was fixed using a mass flowmeter. After the reduction tests, the samples were naturally cooled in the oven using N_2 (99.990%) at a flow rate of ≈ 1 L.min^{-1}. After cooling, the sample was kept in a desiccator for the subsequent XRD analysis. All the gases used in the experiments were supplied by White Martins.

7. Isoconversional Kinetics

The isoconversional method is widely applied for understanding the decomposition, oxidation and reduction reactions of many materials of technological interest (Cheng et al., 2015; Zivkovic et al., 1998; Guimarâes et al., 2016; Olzak et al., 1999; Wang et al., 2018; Pourghahramani, 2007; Tomic et al., 2012). It allows the estimation of the activation energy of a thermal process without the prior knowledge of the involved kinetic model (Chilgi et al., 2014). Its basis relies on the kinetics as shown by the Equation (1) (Vyazovkin et al., 1965):

$$\frac{\partial \alpha}{\partial T} = \frac{A}{\beta} exp\left(\frac{-E_a}{RT}\right) f(\alpha) \qquad (1)$$

Where A and E_a are respectively the pre-exponential factor and activation energy, R is the universal gas constant, T is the absolute temperature, $f(\alpha)$ is the conversion function, β is the heating rate and α is the extent of the conversion of reactants to the products. The isoconversional principle establishes that for a constant extent of conversion (α), the reaction rate is only a function of the temperature (T). The Equation (2) is obtained by rearranging and taking the natural log of both sides of the Equation (1). It is the basis of the differential method of Friedman (Vyazovkin et al., 1965).

$$ln\left(\beta \frac{d\alpha}{dT}\right)_\alpha = ln(A_\alpha \mathrm{f}(\alpha)) - \frac{E_\alpha}{RT_\alpha} \qquad (2)$$

This method requires the differentiation of the curves α versus T, and this procedure usually creates some scattering on the E_α values. Numerical differentiation can be avoided by using integration methods. Equation (3) is the result of the integration of Equation (1):

$$g(\alpha) \equiv \frac{A}{\beta} \int_0^{T_\alpha} exp\left(\frac{-E_\alpha}{RT}\right) dt = \frac{A}{\beta} I(E,T) \quad (3)$$

The integral $I(E, T)$ has no closed-form analytical solution and it is solved by using numerical methods. Two expressions are commonly used as approximate solutions to the integral I(E,T): (i) the Ozawa-Flynn-Wall Solution (OFW) (Equation 4) (Ozawa, 1965; Flynn, 1966) and (ii) the Kissinger-Akahira-Sunose Solution (KAS) (Equation 5) (Coats et al., 1964):

$$\ln(\beta) = 1.0516\left(\frac{E_a}{RT_p}\right) - A' \quad (4) \qquad -ln\left(\frac{\beta}{T_p^2}\right) = \frac{E_a}{RT_p} - ln\left(\frac{A''R}{E_a}\right) \quad (5$$

where A´ and A´´ are constants.

Thermodynamic Data

All the thermodynamic data were obtained from HSC Chemistry 6.0 software.

8. Results

8.1. Chemical / Mineral Composition

The element composition of the ore sample is shown on Table 4 (weight %). The vanadium content is considerably higher compared to other similar studies, where the vanadium ore (VTM) and concentrates were also submitted to reduction process (Li et al., 2019; Zhao et al., 2019). It is noteworthy that a high vanadium content implies less energy for heating and/or melting the gangue, which corroborates the choice of pyrometallurgical routes.

Table 4. Chemical composition of the vanadium ore (weight %).

Elements	Content Percentage(%)
Al	0.72
Ca	0.29
Fe	58.2
K	0.17
Mg	0.79
Mn	0.11
Si	1.47
Ti	4.33
V	1.92

As Table 1 shows, the ore sample presents a high iron content, which is a common feature for vanadium ores. Additionally, the titanium content is relatively low, and as will be discussed later, it was not found in the crystalline network of the magnetite.

Finally, the absence of chromium, an element which is also ordinary for vanadium ores, enables the choice of the reduction method for ferrovanadium alloys production, since this element has deleterious effects on the blast furnace process (BF process) and "pre-reduction roasting magnetic separation process" (Sui et al., 2017). The x-ray patterns and interpretation for the ore sample are shown on Table 5 and Figure 1, respectively. The results reveal that the main mineral constituents are maghemite (52.32%) and magnetite (15.73%), and that most of the iron content (85.8%) is found in these mineral phases. The total iron content estimated from its proportions on the mineral phase is 57.6%, which is close to the elemental composition presented on Table 4 (58.2%).

Table 5. Mineral composition of the vanadium ore sample.

Mineral name	Chemical structure	Content (%)
Tricalcium silicate	Ca_3SiO_5	1.85
Clinopyroxene	$Ca_{0.4}Mg_{1.6}Si_2O_6$	4.22
Cronstedtite	$Fe_4SiO_5(OH)_4$	0.75
Fayalite	Fe_2SiO_4	1.8
Ulvospinel	Fe_2TiO_4	5.93
Greenalite	$Fe_{2.8}Si_{2.2}O_5(OH)_{3.3}$	2.07
Ilmenite	$FeTiO_3$	4.18
Indialite	$Mg_2Al_4Si_5O_{18}$	1.12
Magnesioferrite	$MgFe_2O_4$	5.12
Magnetite	Fe_3O_4	15.73
Maghemite	γFe_3O_4	52.32
Melanovanadite	$CaV_4O_{10}*5H_2O$	3.12
Sudoite	$Mg_{1.9}Fe_{0.3}Al_{3.9}Si_3O_{10}(OH)_{7.9}$	1.81

Figure 1. XRD patterns and Rietveld refinement of the vanadium ore sample. (Cr) cronstedtite; (C) clinopyroxene; (F) fayalite; (U) ulvospinel; (Ca) tricalcium silicate; (G) greenalite; (M) magnetite; (Mh) maghemite; (I) Ilmenite; (In) Indialite; (V) melanovanadite; (Mg) magnesioferrite and (S) sudoite.

Figures 2 and 3 show the scanning electron microscopy (SEM) and EDS mapping images of the ore sample. Both figures show that the vanadium element is diffused all over the mineral phases, which leads to difficulties on the vanadium concentration process by conventional unit operation. Some minerals identified by the XRD analysis were highlighted on Figure 3.

As mentioned before, the EDS mapping do not show the presence of titanium in the crystalline network of magnetite and maghemite.

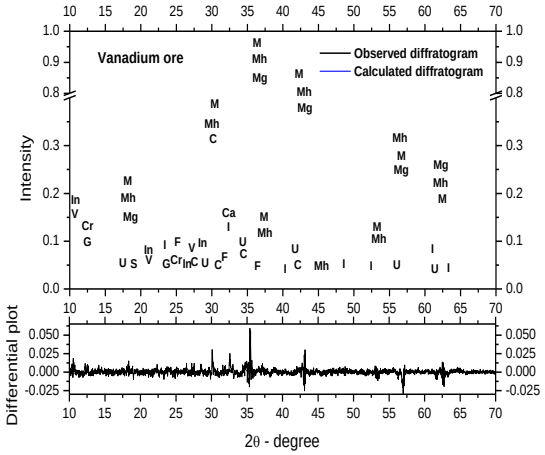

Figure 2. SEM-EDS of the vanadium ore. Left hand side secondary electrons image and right-hand side backscattered electrons image.

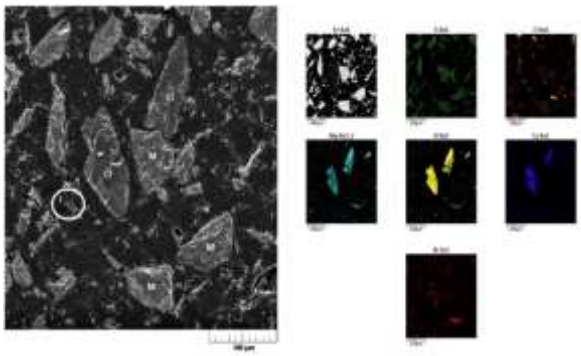

Figure 3. SEM-EDS of the sample. (I) Ilmenite; (Cl) Clinopyroxene and (M) magnetite or maghemite.

8.2. Hydrogen Reduction

The TG and DTG curves of the ore sample submitted to hydrogen reduction are shown on Figure 4. Three thermal events can be identified on these curves, named here as A, B, and C for the TG curve, and A´, B´ and C´ for the DTG curve. After hydrogen reduction, the ore samples were submitted to XRD (Figure 5, 6 and 7) and mineral phases were quantified using the Rietveld method (Table 6).

Figure 4 shows that the thermal event A take place from 350°C to 420ºC, which may be related to the reduction of the thermal decomposition products of the minerals ulvospinel (Fe_2TiO_4) and magnesioferrite ($MgFe_2O_4$). While this thermal decomposition is not thermodynamically favourable at 420°C under an inert atmosphere, as demonstrated by equations (6) and (7), it is favourable for the magnesioferrite when using a reducing atmosphere (Equation 8).

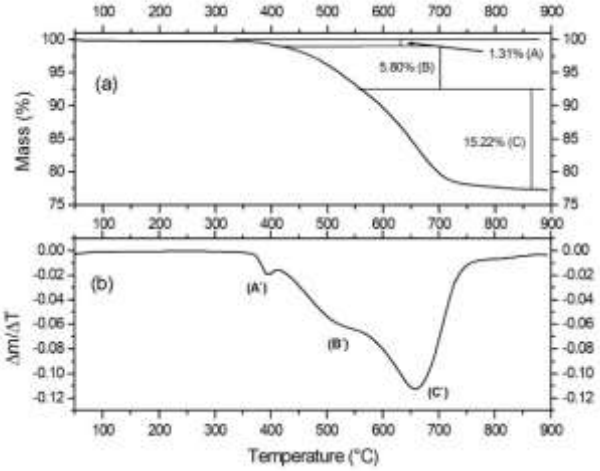

Figure 4. Hydrogen reduction of the ore sample (H_2 = 100ml/min; heating rate = 10°C/min): (a) TG and (b) DTG curves.

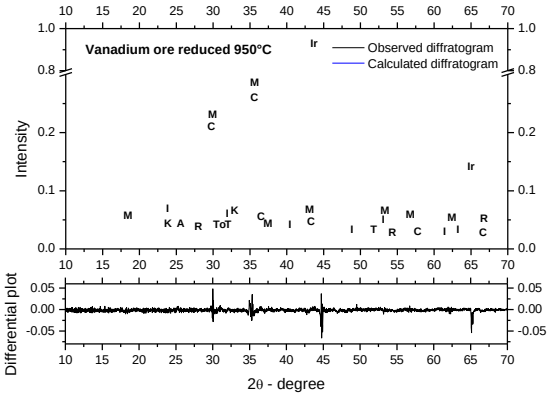

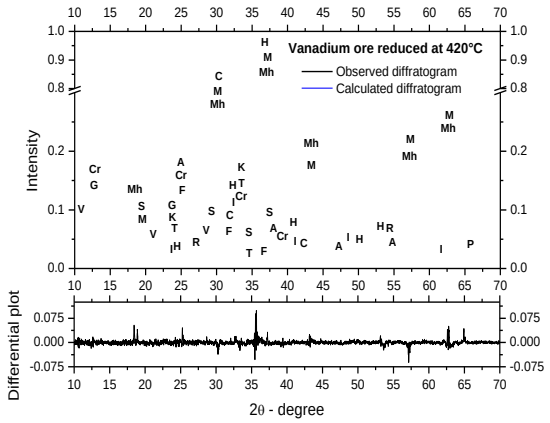

Figure 5. XRD patterns and Rietveld refinement method of the vanadium ore reduced at 420°C. (A) anatase; (C) clinopyroxene; (Cr) cronstedtite; (F) fayalite; (G) greenalite; (H) hematite; (K) karelianite; (I) ilmenite; (M) magnetite; (Mh) maghemite; (V) melanovanadite; (P) pyrope; (R) rutilie; (S) spinel and (T) tristarite.

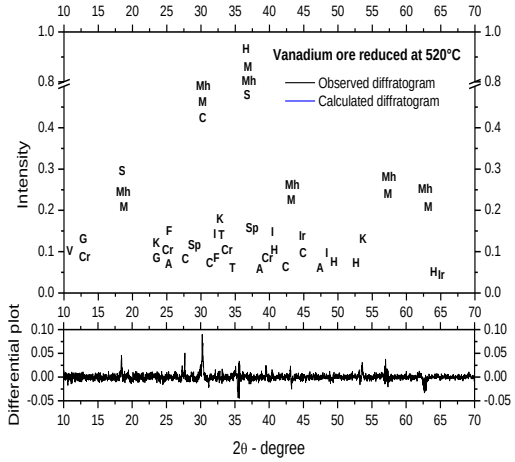

Figure 6. XRD patterns and Rietveld refinement method of the vanadium ore reduced at 520°C. (A) anatase; (C) clinopyroxene; (Cr) cronstedtite; (F) fayalite; (G) greenalite; (H) hematite; (K) karelianite; (I) ilmenite; (Ir) iron; (M) magnetite; (Mh) maghemite; (V) melanovanadite; (Sp) spinel; (S) sudoite and (T) tristarite.

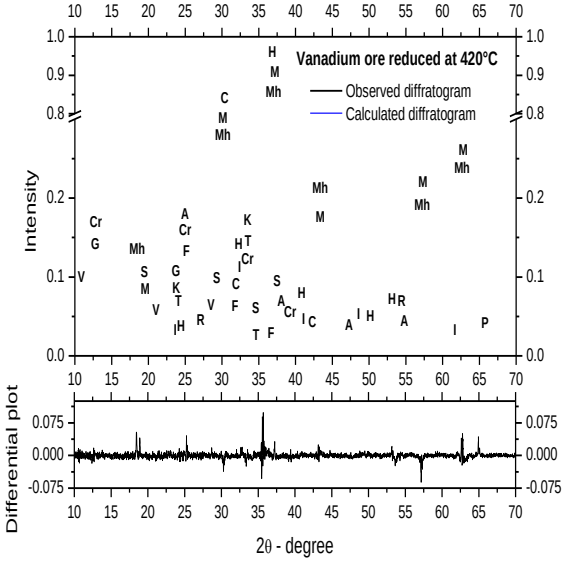

Figure 7. XRD patterns and Rietveld refinement method of the vanadium ore reduced at 950°C. (A) anatase; (C) clinopyroxene; (K) karelianite; (I) ilmenite; (Ir) Iron; (M) Magnetite; (R) Rutile; (To) Ti_7O_{13} and (T) tistarite.

Table 6. Mineral composition of the vanadium ore reduced at different temperatures.

Mineral name	Chemical Structure	Content (%)		
		420° C	520 °C	950° C
Anatase	TiO_2	2.06	0.82	0.61
Clinopyroxene	$Ca_{0.4}Mg_{1.6}Si_2O_6$	3.22	12.51	30.5
Cronstedtite	$Fe_4SiO_5(OH)_4$	1.41	0.54	-
Fayalite	Fe_2SiO_4	1.67	1.35	-
Greenalite	$Fe_{2.8}Si_{2.2}O_5(OH)_{3.3}$	1.85	0.49	-
Hematite	Fe_2O_3	4.36	0.26	-
Karelianite	V_2O_3	2.17	2.86	1.03
Ilmenite	$FeTiO_3$	4.69	4.21	7.47
Iron	Fe	-	1.99	42.26
Magnetite	Fe_3O_4	15.85	16.61	15.34
Maghemite	γFe_3O_4	56.22	38.84	-
Melanovanadite	$CaV_4O_{10}*5H_2O$	3.03	1.46	-
Pyrope	$Mg_3Al_2(SiO_4)_3$	0.3	-	-
Rutile	TiO_2	0.8	-	0.15
Spinel	$Mg(Al,Fe^{3+})_2O_4$	0.58	9.33	-
Sudoite	$Mg_2Al_3(Si_3AlO_{10})(OH)_8$	-	6.16	-
-	Ti_7O_{13}	-	-	1.62
Tistarite	Ti_2O_3	2.05	2.12	1.02

$$MgFe_2O_4 = Fe_2O_3 + MgO$$

$$\Delta G^0 = -0.0164T^2 + 21.04T + 13{,}509 \text{ (J/mol) } (473K < T < 1273K) \quad (6)$$

$$Fe_2TiO_4 = 2FeO + TiO_2$$
$$\Delta G^0 = -2.85T + 38{,}065 \text{ (J/mol) } (473K < T < 1273K) \quad (7)$$

$$3MgFe_2O_4 + H_2(g) = 2Fe_3O_4 + 3MgO + H_2O(g)$$
$$\Delta G^0 = -116.24T + 74{,}562 \text{ (J/mol) } (473K < T < 1273K) \quad (8)$$

It is believed that the thermal decomposition of the ulvospinel occurs as one of the chemical reactions presented from equations (9) through (19). They all represent redox reactions where Fe^{2+} is oxidized to Fe^{3+} by different vanadium oxides.

$$Fe_2TiO_4 + V_2O_5 = Fe_2O_3 + TiO_2 + 2VO_2 \quad (9)$$

$$Fe_2TiO_4 + 2/3V_2O_5 = 2/3Fe_3O_4 + TiO_2 + 4/3VO_2 \quad (10)$$

$$Fe_2TiO_4 + 1/3V_2O_5 = 2/3Fe_3O_4 + TiO_2 + 1/3V_2O_3 \quad (11)$$

$$Fe_2TiO_4 + 3/5V_2O_5 = Fe_2O_3 + TiO_2 + 2/5V_3O_5 \quad (12)$$

$$Fe_2TiO_4 + 1/2V_2O_5 = Fe_2O_3 + TiO_2 + 1/2V_2O_3 \quad (13)$$

$$Fe_2TiO_4 + 3VO_2 = Fe_2O_3 + TiO_2 + V_3O_5 \quad (14)$$

$$Fe_2TiO_4 + 2VO_2 = Fe_2O_3 + TiO_2 + V_2O_3 \quad (15)$$

$$Fe_2TiO_4 + 2VO_2 = 2/3Fe_3O_4 + TiO_2 + 2/3V_3O_5 \quad (16)$$

$$Fe_2TiO_4 + 4/3VO_2 = 2/3Fe_3O_4 + TiO_2 + 2/3V_2O_3 \quad (17)$$

$$Fe_2TiO_4 + 4/3V_3O_5 = 2/3Fe_3O_4 + TiO_2 + 2V_2O_3 \quad (18)$$

$$Fe_2TiO_4 + 2V_3O_5 = Fe_2O_3 + TiO_2 + 3V_2O_3 \quad (19)$$

Figure 8 presents the Ellingham Chart for the reactions (9) through (19), showing that they are thermodynamically favourable at the temperature of the thermal event A. These charts also show that for the same oxidizing agent at the temperature of the event A, with the exception of the oxidation reaction induced by V_3O_5 (equations 18 and 19), the formation of hematite is always more favourable than magnetite. The formation of hematite, in turn, is due to solid reactions among the ore minerals.

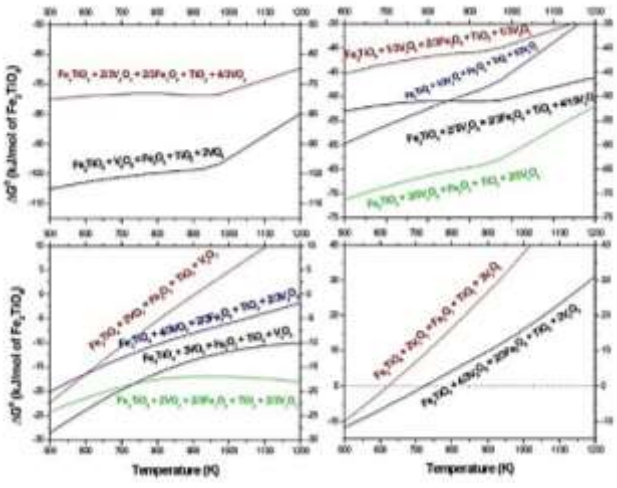

Figure 8. Ellingham chart for decomposition reaction of ulvospinel

The absence of the ulvospinel and magnesioferrite minerals on Table 6 indicates their decomposition induced by reduction, as described by the equations 6 through 19. Consequently, there was an increase in the maghemite content and the formation of hematite, as shown on Table 6 (reduced at 420°C). Table 5 indicates an initial magnesioferrite content of 5.12%, and according to the Equation (8), the expected loss of mass by reduction of this mineral is approximately 0.14% (0.0267 x 5.12%). The mass loss associated with event A is considerably greater than the calculated value and this can be attributed to the partial reduction of the hematite content formed after the decomposition of the ulvospinel.

Finally, Table 6 shows the formation of Tistarite (Ti_2O_3) due to reduction of $FeTiO_3$ or TiO_2, which means that for an atmosphere with $pH_2O/pH_2=10^{-5}$, the reduction of the minerals rutile, anatase and ilmenite is not thermodynamically favourable when the activity of the solid species is 1 (Figure 9). However, the formation of Ti_2O_3 suggests that some solid-state reaction is inducing the reduction of TiO_2 or that the activity of this specie is high enough for the reaction to be spontaneous under the applied experimental conditions. The ilmenite reduction reaction also contributes to the loss mass associated with the event A.

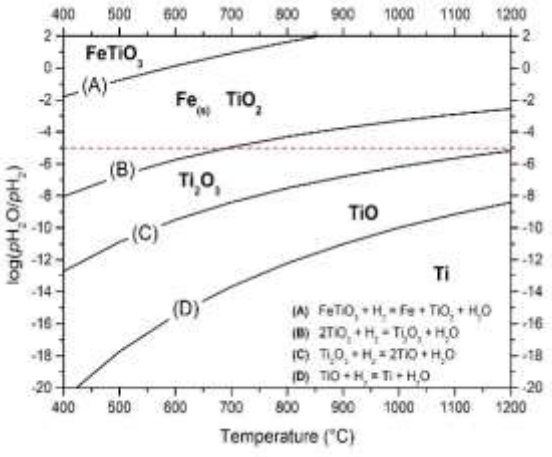

Figure 9. Diagram log(pH_2O/pH_2) vs Temperature for the Fe-Ti-O-H system. The dashed red line represents the experimental conditions of this study

Dehydroxilation of cronstedtite, sudoite and greenalite phyllosilicates occurs in the temperature range of 550°C

to 800°C (events B and C) (Dlugogorski et al., 2014). These minerals are minor components of the ore and undertake different thermal decomposition mechanisms that can produce different mineral phases (Dlugogorski et al., 2014). Therefore, the serpentine mineral will be used as a reference phyllosilicate for the dehydroxilation reaction, as shown on Equation (20). However, this equation cannot be used for the mass loss calculations associated with these thermal transformations.

$$Mg_3(Si_2O_5)(OH)_4 = Mg_2SiO_4 + MgSiO_3 + 2H_2O(g)$$
$$\Delta G^0 = -286T + 136890 \text{ (J/mol)} \qquad (20)$$

The XRD results (Table 6) are evidence that at the temperatures of 520°C to 950°C these minerals are dehydroxylated.

In addition to the thermal decomposition of the phyllosilicates, events B and C are related to the reduction of magnetite and maghemite, as demonstrated by the Equation 21.

$$Fe_3O_4 + 2H_2(g) = 3Fe^0 + 4H_2O(g) \qquad (21)$$

For a sample composed of 68.05% of magnetite + maghemite, the theoretical mass loss associated with the reduction of these minerals is 18.8% (0.2764 X 68.05%). As can be seen on Figure 4, the actual mass loss was found to be 21.02%, which is a bit higher than the theoretical estimation.

Notwithstanding, like the iron oxides, the vanadium and titanium oxides will also be reduced by a reducing atmosphere with $\log(pH_2O/pH_2) = -5$ (Figures 10 and 11). The reduction of oxidized minerals phases of vanadium, titanium and iron is confirmed by the results shown on Table 6.

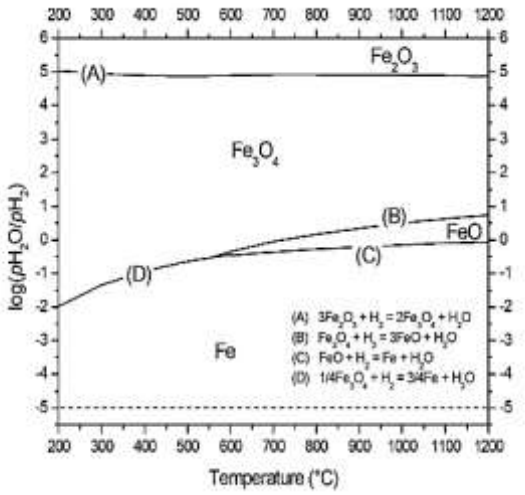

Figure 10. Diagram log(pH_2O/pH_2) vs Temperature for the Fe-O-H system. The dashed red line represents the experimental conditions of this study.

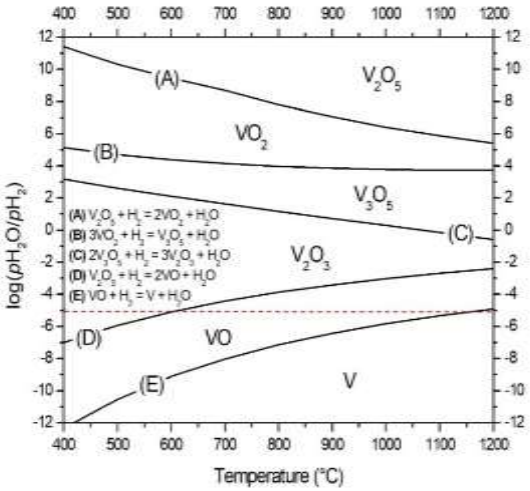

Figure 11. Diagram log(pH_2O/pH_2) vs Temperature for the V-O-H system. The dashed red line represents the experimental conditions of this study.

Figure 12 shows an SEM-EDS image of the ore sample reduced at the temperature of 950°C. It can be noticed the high porosity of the solid particles, and these pores were generated by the gaseous product of the reaction (H_2O).

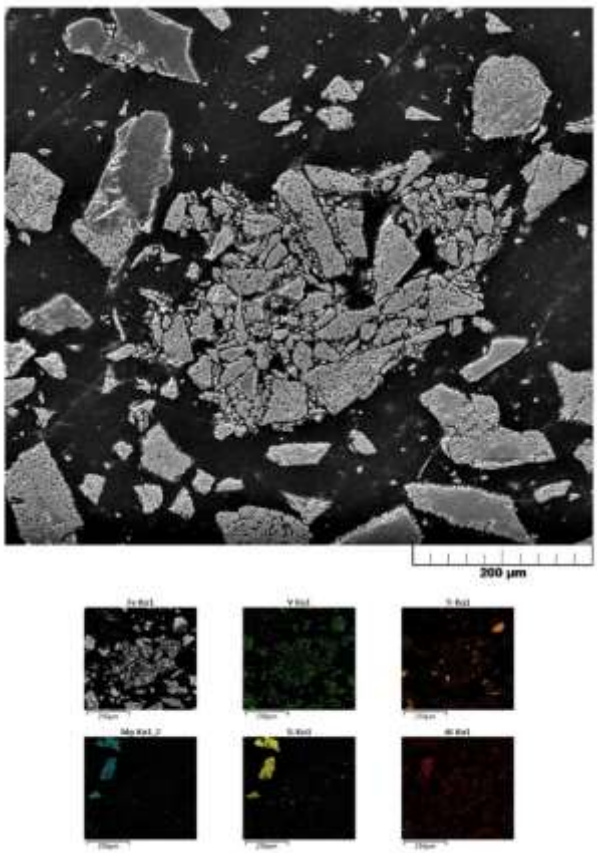

Figure 12. SEM-EDS images of the ore sample reduced at 950°C by hydrogen (1h – 1L/min).

8.3. Isoconversional Kinetics

As mentioned before, the integral isoconversional method was used to evaluate the kinetics of the ore sample reduction. Figure 13 shows the reduction curves at different heating rates (β).

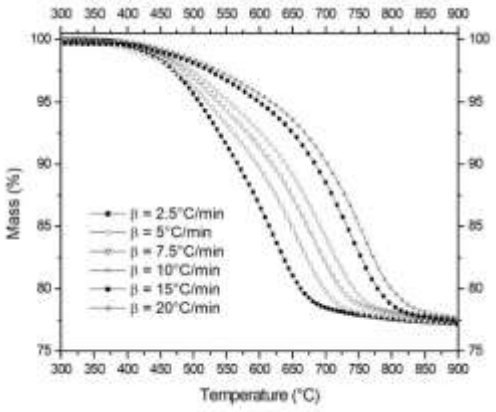

Figure 13. TG curves for the ore sample under different heating rates (β).

The extent of conversion (α) was calculated using the initial content of maghemite and magnetite (P_0 = *68.8%*) in the ore sample, as shown on Equation (22). A value of α 1 indicates that 100% of these minerals have been reduced to metallic iron.

$$\alpha = \frac{w_t}{\left(1-\frac{3\times MM_{Ir}}{MM_{mag}}\right)\times\frac{P_0}{100}} \quad (22)$$

Where MM_{Ir} and MM_{Mag} are respectively the molar masses of iron and magnetite (or maghemite) and w_t is the mass loss at a specific time.

Figure 14 depicts the plots of the integration methods OFW (Equation 4) and KAS (Equation 5), using three different α values. Table 7 shows the apparent activation energy of these plots and the coefficient of determination (R^2) of the linear regression fit.

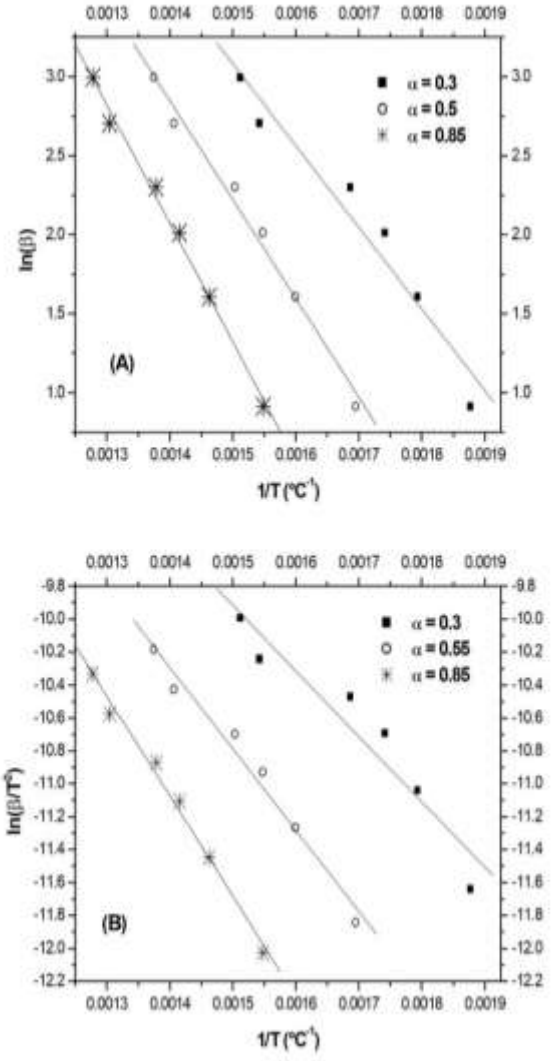

Figure 14. Plots of (A) Ozawa-Flynn-Wall method and (B) Kissinger-Akahira-Sunose methods using three different values of α.

Table 7. Apparent activation energy for different conversion (α) values calculated using the OFW and KAS integration methods.

Conver-sion (α)	OFW		KAS	
	E_a/kJ mol^{-1}	R^2	E_a/kJ mol^{-1}	R^2
0.10	51.66	0.8857	40.56	0.8388
0.15	47.28	0.9015	35.97	0.8513
0.20	44.79	0.9155	33.24	0.8648
0.25	44.28	0.9328	32.44	0.8878
0.30	45.21	0.9506	33.06	0.9152
0.35	46.89	0.9651	34.43	0.9393
0.40	48.86	0.9752	36.09	0.9565
0.45	50.86	0.9815	37.79	0.9674
0.50	52.78	0.9852	39.46	0.9741
0.55	54.70	0.9875	41.08	0.9782
0.6	56.50	0.9891	42.63	0.9811
0.65	58.26	0.9904	44.15	0.9835
0.70	60.03	0.9917	45.68	0.9858
0.75	61.86	0.9928	47.28	0.9878
0.80	63.79	0.9938	48.96	0.9894
0.85	65.75	0.9973	50.67	0.9908
0.90	67.75	0.9950	52.37	0.9916
0.95	70.36	0.9956	54.59	0.9927
1.0	82.47	0.9844	65.54	0.9781

Figure 15 presents a plot of the apparent activation energy (E_a) as a function of the extent of conversion (α). The E_a values ranged from 44.28kJ.mol^{-1} to 82.47kJ.mol^{-1} for the OSW method and from 33.44kJ.mol^{-1} to 65.54kJ.mol^{-1} when the KAS method was applied. The E_a values suggest that the slow process step is a mixed step for low conversion value and a chemical step for high conversion values.

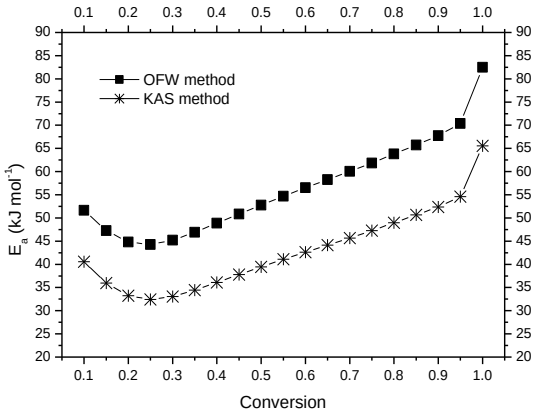

Figure 15. Apparent activation energy (E_a) estimated by the OFW and KAS integration methods.

9. Conclusions

A sample of vanadium ore was extensively characterized by x-ray diffraction, elemental analysis, and Electron Microscopy-Energy Dispersive Spectroscopy (SEM-EDS).

The major mineral phases were found to be maghemite and magnetite. SEM-EDS showed that vanadium is diffused through the crystalline network of almost all minerals of the ore sample.

The ore reduction was assessed by hydrogen thermogravimetry (TG). TG curves revealed that the mineral magnesioferrite is decomposed at temperatures close to 420°C, and its thermal decomposition products are subsequently reduced by the hydrogen gas.

TG curves suggest also that the mineral ulvospinel is decomposed by a redox reaction between this mineral and the different vanadium oxides of the ore sample. In addition, the products of this redox reaction are also reduced by the hydrogen gas at temperatures close to 420°C. The mineral maghemite was reduced to metallic iron and most of the mass loss of the ore as the result of the hydrogen reduction process was related to this reaction.

The use of the integral isoconversional methods KAS and OFW resulted in good linear determination coefficients (R^2). The estimated apparent activation energy (E_a) values ranged from 44.28kJ.mol^{-1} to 82.47kJ.mol^{-1} when the KAS method was used and from 33.44kJ.mol^{-1} to 65.54kJ.mol^{-1} for the OFW method.

These values imply a mixed controlled step for low conversion values and chemical controlled step for high conversion values.

Acknowledgements

The financial support to this research was provided by the agencies Fundação de Amparo à Pesquisa do Estado de Minas Gerais (FAPEMIG) and Conselho Nacional de Desenvolvimento Científico e Tecnológico (CNPq). The characterization analysis was performed by REDEMAT, which is gratefully appreciated.

References

Barth, T. F., & Posnjak, E. (1932). Spinel structures: with and without variate atom equipoints. *Zeitschrift Für Kristallographie-Crystalline Materials*, *82*(1-6), 325-341.

Barth, T.F.W., Posnjak, E. (1934). The crystal structure of ilmenite Locality: Quincy, Massachusetts. *USA Zeitschrift fur Kristallographie*, 88, 265-270.

Bosi, F., Halenius, U., Skogby, H. (2009). Crystal chemistry of the magnetite-ulvospinel series. *American Mineralogist*, 94, 181-189.

Cheng, G.J., Liu, J.X., Liu, Z.G., Chu, M.S., Xue, X.X. (2015). Non-isothermal reduction mechanism and kinetics of high chromium vanadium-titanium magnetite pellets. *Ironmaking and Steelmaking*, 42, 17-26.

Cilgi, G. K., Cetişli, H., & Donat, R. (2014). Thermal and kinetic analysis of uranium salts. *J. of Thermal Analysis and Calorimetry*, 115(2), 2007-2020.

Coats, A.W., Redfern, J.P. (1964). Kinetic Parameters from Thermogravimetric Data. *Nature*, 201, 68-69.

Dlugogorski, B.Z., Balucan, R.D. (2014). Dehydroxylation of serpentine minerals: Implications for mineral carbonation. *Renewable and Sustainable Energy Reviews*, 31, 353-367.

Eggleston, R. A., & Bailey, S. W. (1967). Structural aspects of dioctahedral chlorite. *American Mineralogist: Journal of Earth and Planetary Materials*, *52*(5-6), 673-689.

Fleet, M. E. (1986). The structure of magnetite: Symmetry of cubic spinels. *Journal of Solid State Chemistry*, *62*(1), 75-82.

Flynn, J. H., & Wall, L. A. (1966). General treatment of the thermogravimetry of polymers. *Journal of research of the National Bureau of Standards. Section A, Physics and chemistry*, *70*(6), 487-523.

Ganguly, J., Cheng, W., & O'Neill, H. S. C. (1993). Syntheses, volume, and structural changes of garnets in the pyrope-grossular join: Implications for stability and mixing properties. *American Mineralogist*, *78*(5-6), 583-593.

Gasik, M. (Ed.). (2013). *Handbook of ferroalloys: theory and technology*. Butterworth-Heinemann.

Gilligan, R., & Nikoloski, A. N. (2020). The extraction of vanadium from titanomagnetites and other sources. *Minerals Engineering*, *146*, 106106.

Golovastikov, N. I. (1975). Crystal structure of tricalcium silicate, 3CaOSiO_2= C_3S. *Sov. Phys. Crystallogr.*, 20(4), 441-445.

Guimarâes, D., Oliveira, V.D.A., Leao, V.A. (2016). Kinetics and thermal decomposition of ettringite synthesized from aqueous solutions. *J. of Thermal Analysis and Calorimetry*, 124, 1679-1689.

Hazen, R. M. (1977). Effects of temperature and pressure on the crystal structure of ferromagnesian olivine. *American Mineralogist*, *62*(3-4), 286-295.

Hendricks, S. B. (1939). Random structures of layer minerals as illustrated by cronstedite (2FeO. Fe2O3. SiO. 2.2 H2O). Possible iron content of kaolin. *American Mineralogist: Journal of Earth and Planetary Materials*, *24*(9), 529-539.

Horn, M. S. C. F., Schwebdtfeger, C. F., & Meagher, E. P. (1972). Refinement of the structure of anatase at several temperatures. *Zeitschrift für Kristallographie-Crystalline Materials*, *136*(1-6), 273-281.

Kim, S.M.D.E. (1969). Lattice constants, thermal expansion coefficients, densities, and imperfections in gold and the alphaphase of the gold-indium system, Z. Metallkunde, 69, 272-277.

Konnert, J. A., & Evans, H. T. (1987). Crystal structure and crystal chemistry of melanovanadite, a natural vanadium bronze. *American M.*, *72*(5-6), 637-644.

Le Page, Y., & Strobel, P. (1982). Structural chemistry of the Magnéli phases TinO2n− 1, 4≤ n≤ 9: II. Refinements and structural discussion. *Journal of Solid-State Chemistry*, *44*(2), 273-281.

Li, W., Fu, G., Chu, M., & Zhu, M. (2019). Effect of porosity of Hongge vanadium titanomagnetite-oxidized pellet on its reduction swelling behavior and mechanism with hydrogen-rich gases. *Powder Technology*, *343*, 194-203.

Liu, S. S., Guo, Y. F., Qiu, G. Z., & Jiang, T. (2014). Solid-state reduction kinetics and mechanism of pre-oxidized vanadium–titanium magnetite concentrate. *Transactions of nonferrous metals society of china*, *24*(10), 3372-3377.

Meagher, E.P., Lager, G.A. (1979). Polyhedral thermal expansion in the TiO2 polymorphs: Refinement of the crystal structure of rutile and brookite at high temperature. *The Canadian Mineralogist*, 17, 77-85.

Moskalyk, R. R., & Alfantazi, A. M. (2003). Processing of vanadium: a review. *Minerals engineering*, *16*(9), 793-805.

NEWNHAM, E., & DE HAAN, Y. M. (1962). Refinement of the a Al2O3, Ti2O3, V2O3 and Cr2O3 structures. *Zeitschrift für Kristallographie-Crystalline Materials*, *117*(1-6), 235-237.

Olszak-Humienik, M., & Możejko, J. (1999). Kinetics of thermal decomposition of dolomite. *Journal of thermal analysis and calorimetry*, *56*(2), 829-833.

Ozawa, T. (1965). A new method of analyzing thermogravimetric data. *Bulletin of the chemical society of Japan*, *38*(11), 1881-1886.

Passerini, L. (1930). Ricerche sugli spinelli. II. I composti: CuAl2O4; MgAl2O4; MgFe2O4; ZnAl2O4; ZnCr2O4; ZnFe2O4; MnFe2O4. *Gazz Chim Ital*, *60*, 389-399.

Pecharromán, C., González-Carreño, T., Iglesias, J.E. (1995). The infrared dielectric properties of maghemite, γ-Fe2O3, from reflectance measurement on pressed powders. *Physics and Chemistry of Minerals*, 22, 21-29.

Peng, H. (2019). A literature review on leaching and recovery of vanadium. *Journal of Environmental Chemical Engineering*, *7*(5), 103313.

Pourghahramani, P., & Forssberg, E. (2007). Reduction kinetics of mechanically activated hematite concentrate with hydrogen gas using nonisothermal methods. *Thermochimica acta*, *454*(2), 69-77.

Princivalle, F., Martignago, F., Nestola, F., Negro, A.D. (2012). Kinetics of cation ordering in synthetic Mg(Al, Fe3+)2O4 spinels. *European Journal of Mineralogy*, 24, 633-643.

Redhammer, G. J., Tippelt, G., Roth, G., & Amthauer, G. (2004). Structural variations in the brownmillerite series Ca2 (Fe2− x Al x) O5: Single-crystal X-ray diffraction at 25° C and high-temperature X-ray powder diffraction (25° C≤ T≤ 1000° C). *American M.*, 89(2-3), 405-420.

Rezaee, M., Khoie, S. M. M., & Liu, K. H. (2011). The role of brookite in mechanical activation of anatase-to-rutile transformation of nanocrystalline TiO 2: An XRD and Raman spectroscopy investigation. *CrystEngComm*, *13*(16), 5055-5061.

Schwartz, K. B., Leong, D. B., & McConville, R. L. (1994). Structural chemistry of synthetic cordierite: evidence for solid solutions and disordered

compositional domains in Bi-flux-grown Mg-cordierites. *Physics and Chemistry of minerals*, *20*(8), 563-574.

Shirozu, H., & Bailey, S. W. (1965). Chlorite polytypism: III. Crystal structure of an orthohexagonal iron chlorite. *American Mineralogist: Journal of Earth and Planetary Materials*, *50*(7-8), 868-885.

Sui, Y. L., Guo, Y. F., Jiang, T., & Qiu, G. Z. (2017). Reduction kinetics of oxidized vanadium titano-magnetite pellets using carbon monoxide and hydrogen. *Journal of Alloys and Compounds*, *706*, 546-553.

Tomic-Tucakovic, B., Majstorovic, D., Jelic, D., Mentus, S. (2012). Thermogravimetric study of the kinetics of Co3O4 reduction by hydrogen. *Thermochimica Acta*, 541, 15-24.

Tsirel'Son, V. G., Antipin, M. Y., Strel'Tsov, V. A., Ozerov, R. P., & Struchkov, Y. T. (1988, February). Electron density distribution and electric field gradient in hematite at 153 K determined from precision X-ray diffraction data. In *Soviet Physics Doklady* (Vol. 33, p. 89).

Vyazovkin, S., Isoconversional Kinetics, in: M.E. Brown, P.K. Gallagher (Eds.) *Handbook of Thermal Analysis and Calorimetry*, Elsevier B.V., Amsterdam, 2008, pp. 503-538.

Wang, M., Chen, B., Huang, S., Wang, X., Liu, B., Ge, Q., & Xie, S. (2017). A novel technology for vanadium and chromium recovery from V-Cr-bearing reducing slag. *Hydrometallurgy*, *171*, 116-122.

Wang, X., Gao, D., Chen, B., Meng, Y., Fu, Z., & Wang, M. (2018). A clean metallurgical process for separation and recovery of vanadium and chromium from V-Cr-bearing reducing slag. *Hydrometallurgy*, *181*, 1-6.

Wang, X., Wang, X., Shao, Y., Jin, Z., & Jin, B. (2018). Reactivity of a Chinese lean iron ore as oxygen carrier Kinetics & characterization. *Thermochimica Acta*, *670*, 114-122.

Xiang, J., Huang, Q., Lv, W., Pei, G., Lv, X., & Bai, C. (2018). Recovery of tailings from the vanadium extraction process by carbothermic reduction method: Thermodynamic, experimental and hazardous potential assessment. *J. of hazardous materials*, *357*, 128-137.

Xiao, Y., Jalkanen, H., Yang, Y., Mambote, C. R., & Boom, R. (2010). Ferrovanadium production from petroleum fly ash and BOF flue dust. *Minerals Engineering*, *23*(14), 1155-1157.

Zhang, B., Liu, C., Liu, Z., Li, Z., Jiang, M. (2019). Remediation of the vanadium slag processing residue and recovery of the valuable elements. *Process Safety and Environmental Protection*, 128, 362-371.

Zhang, Y., Zhang, T. A., Dreisinger, D., Lv, C., Lv, G., & Zhang, W. (2019). Recovery of vanadium from calcification roasted-acid leaching tailing by enhanced acid leaching. *Journal of hazardous materials*, *369*, 632-641.

Zhao, W., Chu, M., Wang, H., Liu, Z., Tang, J., & Ying, Z. (2019). Reduction behavior of vanadium-titanium magnetite carbon composite hot briquette in blast furnace process. *Powder technology*, *342*, 214-223.

Živković, Ž. D., & Šesták, J. (1998). Kinetics and mechanism of the oxidation of molybdenum sulphide. *Journal of thermal analysis and calorimetry*, *53*(1), 263-267.